Graphene anchored with Fe_3O_4 nanoparticles as anode for enhanced Li-ion storage

Marappan Sathish*, Takaaki Tomai, Itaru Honma*

Institute of Multidisciplinary Research for Advanced Materials, Tohoku University, 2-1-1, Katahira, Aoba-Ku, Sendai 980-8577, Japan

HIGHLIGHTS

► Fe_3O_4/GNS nanocomposites were prepared at very dilute and hydrothermal condition.
► Effect of Fe_3O_4/GNS ratio on the Li-ion storage capacity has been examined.
► High reversible capacity of 930 and 675 mAh g^{-1} was attained for 2nd and 50th cycles, respectively.
► Enhanced performance was attributed to the advantages of the electrodes' structure

ARTICLE INFO

ABSTRACT

Magnetite (Fe_3O_4) nanoparticles anchored graphene nanocomposites with different weight ratios of Fe_3O_4 and graphene nanosheets (GNSs) were prepared using hydrothermal method. The X-ray diffraction (XRD) pattern of the prepared nanocomposite reveals the presence of face centered cubic hexagonal crystalline Fe_3O_4 nanoparticles. Raman spectroscopic studies of the nanocomposites confirm the co-existence of Fe_3O_4 and graphene. The electron microscopy images of the nanocomposites revealed the formation of homogeneous nanocrystalline Fe_3O_4 particles on GNS surface. Among the three studied weight ratios (28:72, 40:60 and 60:40), the charge–discharge profile of the nanocomposite electrodes indicates that nanocomposite with 40:60 wt% of Fe_3O_4 and GNS as high capacity (930 mAh g^{-1}) electrode for the lithium-ion (Li-ion) storage. And, the Li-ion storage capacity of the above nanocomposite is much higher than the pure GNS and Fe_3O_4 nanoparticle electrodes. The charge–discharge cycling study indicates that the Fe_3O_4/GNS (40:60) nanocomposite electrode has very high reversible capacity of 675 mAh g^{-1} with columbic efficiency of 97% after 50 cycles. The rate performance of the Fe_3O_4/GNS (40:60) nanocomposite electrode shows high reversible capacities at high rates due to the high conductive GNS support. The cyclic voltammetry experiment reveals the irreversible and reversible Li-ion storage in Fe_3O_4/GNS during the first and subsequent cycles.

© 2012 Elsevier B.V. All rights reserved.

1. Introduction

Commercial lithium-ion (Li-ion) batteries consist of $LiCoO_2$ as positive electrode and graphite as negative electrode have been widely utilized as portable power sources for electronic devices. Recent researches have been focused on improving the power and energy densities of the cathode and anode materials for their promising application in electric vehicles and heavy electric vehicles [1,2]. In addition, reducing the cost, eco-friendly and improving the safety of the electrode materials are essential for their viable use. Metal, metal oxides and metal sulfides such as Sn, Si, SnO_2, Iron oxide and SnS_2 are extensively investigated as possible alternative to replace the graphite anode, which has an inherent limitation with a theoretical gravimetric capacity of 372 mAh g^{-1} [3–10]. Sn and Si based materials show a large theoretical capacity value due to the formation of Li–Sn or Li–Si alloy, respectively [11,12]. However, the large volume expansion/contraction (during charging and discharging) limits their application in Li-ion battery and various researches are under development to overcome the above issues. Thus, the practical application of these materials has been not attained so far. Fe_3O_4 has been widely investigated as one of the most promising anode materials for lithium-ion batteries due to its high theoretical specific capacity (924 mAh g^{-1}), higher operating potential than graphite (reduces the potential safety problems with metallic lithium deposition on the host anode during rapid charge),

high electronic conductivity, low cost and eco-friendliness [13–16]. However, their practical application in lithium-ion batteries is limited by the huge volume change during Li insertion/extraction process that leads to poor cycling performance.

To overcome the above issues, attempts have been made to prepare nanostructured materials with diverse morphologies [2,4]. While, reducing the particle size will increase the surface to volume ratio and that would decrease the volume changes during the Li-ion insertion and extraction. However, aggregation of Fe_3O_4 nanoparticles into bulk particle is another issue to surmount the poor cycling performance. Thus, anchoring the individual Fe_3O_4 nanoparticles homogeneous on electrochemically active or conductive, high surface area support is essential. The recent progress in graphene nanosheets (GNSs) as high surface area and good conductive support for nanocomposite electrode materials [17,18] validates that GNS would be a better support for Fe_3O_4 nanoparticles. The availability of large surface area in the GNS facilitates the homogeneous distribution of nanoparticle on its surface. And, the wobbly arranged Fe_3O_4 anchored GNS is suitable for both intercalation of Li-ions and the compensation of the alloying/dealloying volume change. Thus, Li-ion diffusion length is reduced and the Li-ion can easily access entire surface of GNS and the Fe_3O_4 nanoparticles and the resulting volume change could be easily controlled without any structural damage. Recently, metal oxides/GNS nanocomposites have been successfully prepared using different synthetic strategies and demonstrated for various applications [19–22]. Particularly, SnO_2/GNS and Fe_2O_3 and Fe_3O_4 nanocomposite electrodes have been prepared and their Li-ion storage properties have been reported [23–31]. Interestingly, GNS itself has Li-ion storage capability that offers further advantages to these nanocomposites consists of nanoparticle/GNS. Also, the dispersion of nanoparticle on the GNS hinders the re-stacking of GNS that would also increase the Li-ion storage capacity of GNS. In this present study, Fe–GNS was prepared in the first step at very dilute condition, followed by precipitation of Fe_3O_4 nanoparticles on GNS surface directly by hydrolysis and hydrothermal condition. The homogeneous precipitated of Fe_3O_4 nanoparticle directly on Fe anchored GNS surface was characterized using XRD, TEM, TG and micro-Raman measurements. The electrochemical response of the prepared nanocomposite electrodes was studied using cyclic voltammetry and galvanostatic charge–discharge measurements.

2. Experimental section

2.1. Graphene oxide

Graphene oxide dispersion (15 mg mL^{-1}) was prepared by modified Hummers and Offeman's method reported elsewhere [32,33]. In a typical preparation, 0.5 g of graphite powder (Sigma Aldrich, 5–20 μm), 0.5 g of $NaNO_3$, and 23 mL of H_2SO_4 were stirred together in an ice water bath. Then, 3 g of $KMnO_4$ was slowly added. Once mixed, the solution was transferred to a 35 ± 5 °C water bath and stirred for about 1 h, forming a thick paste. 40 mL of water was added to the above paste and the resulting solution was stirred for 30 min while the temperature was raised to 90 ± 5 °C. Finally, 100 mL of water containing 3 mL of H_2O_2 was added, the color of the solution turns from dark brown to yellow. The warm solution was then filtered and washed with 200 mL of water. The filter cake was then dispersed in water by mechanical agitation. Low-speed centrifugation was done at 1000 rpm for 5 min and the visible particles were removed completely from the precipitates. The supernatant then underwent two more high-speed centrifugation steps at 8000 rpm for 15 min to remove small GO pieces and water-soluble by-products.

The final sediment was re-dispersed in water with mechanical agitation and mild sonication, giving a solution of exfoliated GO.

2.2. Fe_3O_4/GNS synthesis

In a typical preparation, calculated amount of $FeCl_3 \cdot 6H_2O$ (Wako, Japan) in 50 mL water was added to graphene oxide solution (400 mL, ∼0.5 mg mL^{-1}), followed by 100 mg of L(+) ascorbic acid in 50 mL water and the solution was stirred for 30 min vigorously and ultrasonicated for 30 min. Then, ∼5 mL of NH_4OH (Wako, Japan) solution was added drop wise and the resulting mixture was stirred for another 30 min and ultrasonicated for 30 min. The volume of the solution (∼505 mL) was reduced to 30 mL by rotary evaporator at elevated temperature and reduced pressure, and the final solution was put in to Teflon lined stainless steel autoclave and heat treated at 180 °C for 15 h. The resulting nanocomposite powder was washed with ethanol and water, and dried at 60 °C overnight. Fe_3O_4 loading on GNS has been varied by altering the concentration of $FeCl_3 \cdot 6H_2O$ and keeping the GO solution as constant.

2.3. Material characterization

XRD patterns were collected on a RIGAKU (RINT2000 Tokyo, Japan) diffractometer using Ni-filtered Cu-K$_\alpha$ radiation ($\lambda = 1.5418$ Å). TG experiments (SII, TG/DTA 6300) were conducted in a temperature range of 25–800 °C and in an air atmosphere using ∼5–10 mg of the sample at the heating rate of 10 °C min^{-1}. The morphology of the nanocomposites was observed using a Hitachi-4800 field-emission scanning electron microscope (FE-SEM). Scanning and high-resolution transmission electron micrographs (STEM and HR-TEM) were recorded with a JEOL JEM-2100F microscope, working at an accelerating voltage of 200 kV. The structure of the obtained nanocomposites was characterized using a micro-Raman system (HORIBA Scientific, Japan) equipped with a semiconducting laser with a wavelength of 532 nm.

2.4. Electrochemical evaluation

The working electrodes were fabricated by mixing 85 wt% active materials, 10% of acetylene black and 5 wt% polytetrafluoroethylene (used as a binder, PTFE, Sigma Aldrich) and pressed on Ni mesh. The electrodes were dried in a vacuum oven at 160 °C for 3 h before transferring into an Argon-filled glove box. Conventional three electrode cells were fabricated using lithium metal as the counter electrode and reference electrode, and $LiClO_4$ (1 M) in ethylene carbonate/diethyl carbonate (EC/DEC, 1:1 vol%) as the electrolyte. The electrochemical performances of the prepared electrodes were characterized by cyclic voltammetry (Solartron 1260, USA) and galvanostatic charge–discharge (HOKUTO DENKO, Japan) test between 0.001 V and 3 V vs Li/Li$^+$.

3. Results and discussion

The preparation of Fe_3O_4/GNS nanocomposites involves two steps, in the first step anchoring Fe-ions on graphene sheets through the functional group on the GO surface was carried out at very dilute condition, where only presence of GO monolayers was expected. Then, the addition of L(+) ascorbic acid in the second step results the reduction of unutilized functional groups partly. Finally, NH_4OH was added and the volume of the solution was reduced to 30 mL and subjected into hydrothermal condition for Fe_3O_4 formation directly GNS surface. In Fig. 1, the XRD pattern of Fe_3O_4/GNS nanocomposites with different loadings of Fe_3O_4 was compared. In all the nanocomposites, diffraction line
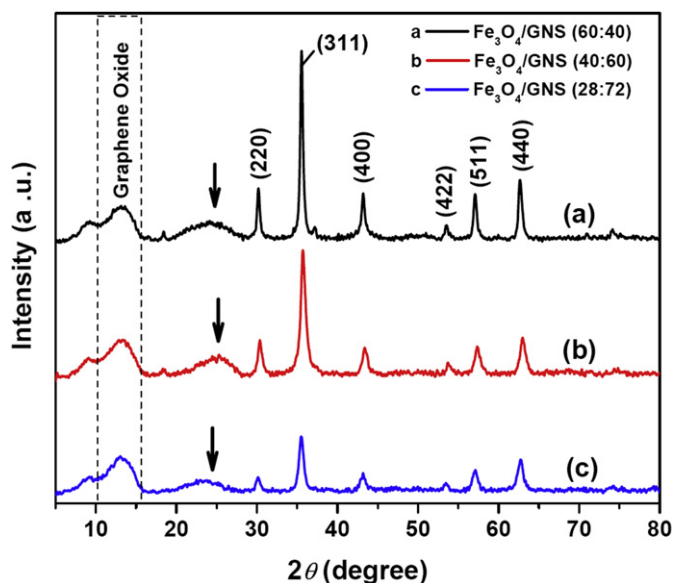
Fig. 1. XRD pattern of Fe$_3$O$_4$/GNS nanocomposites with different weight ratios (a) 60:40, (b) 40:60 and (c) 28:72.

Fig. 2. Raman spectra of (a) Fe$_3$O$_4$ nanoparticles, (b) Fe$_3$O$_4$/GNS (60:40), (c) Fe$_3$O$_4$/GNS (40:60), (d) Fe$_3$O$_4$/GNS (28:72) nanocomposites and (e) pure GNS prepared using the same experimental condition.

corresponding to GO could be seen at $2\theta = 10-15°$, this clearly indicates that the GO was not completely reduced during reduction by hydrazine solution [34]. Also, it hints that the Fe$_3$O$_4$ nanoparticles are attached to graphene sheets chemically through the functional groups on the surface. Thus, the graphene sheets could not re-stack as like graphite and the d spacing value retains similar to the GO. The Fe$_3$O$_4$/GNS nanocomposite (Fig. 1a) shows clear diffraction lines corresponding to face centered cubic structure of magnetite Fe$_3$O$_4$ with a calculated lattice parameter of $a = 8.37$ Å [JCPDS 19-0629]. When compared to GO peak, the intensity of the peaks corresponding to Fe$_3$O$_4$ nanoparticles increases with increasing the loading of Fe$_3$O$_4$ on the GNS (Fig. 1c-a). The crystallite size of Fe$_3$O$_4$ nanoparticle in the Fe$_3$O$_4$/GNS nanocomposite (40:60) was calculated using Debye−Scherrer equation [35], and the calculated crystallite size is ∼15 nm. There is no sharp peak observed for the reduced GNS in all the three Fe$_3$O$_4$/GNS nanocomposites that clearly indicates the absence of GNS re-stacking. However, a broad hump was observed as shown by arrow mark around $2\theta = 25°$ corresponding to disorderly or loosely packed GNS in the Fe$_3$O$_4$/GNS nanocomposite.

The structural and electronic properties of GNS in the nanocomposite have been investigated using laser Raman spectroscopy. Fig. 2 shows Raman spectra of all the nanocomposites, pure GNS (prepared under the same experimental condition), and Fe$_3$O$_4$ nanoparticle prepared without GNS. Raman lines observed for the Fe$_3$O$_4$ nanoparticles (Fig. 2a) indicates the existence of α-Fe$_2$O$_3$ nanoparticles [36,37]. The presence of α-Fe$_2$O$_3$ nanoparticles can be attributed to the decomposition of Fe$_3$O$_4$ nanoparticles by the strong laser light used in Raman spectroscopic measurements. Similar observations are reported for the Fe$_3$O$_4$ to the hematite phase of Fe$_2$O$_3$ at high laser intensity during Raman measurement [36,37]. The characteristic D and G bands observed for the nanocomposites (Fig. 2b−d) and pure GNS (Fig. 2e) at 1345 and 1584 cm^{-1} are in good correspondence with the reported values in the literature (1350 and 1585 cm^{-1}), respectively [38,39]. The D band is associated with disordered samples or graphene edges, while the G band is the result of the first-order scattering of the E_{2g} mode of sp^2 carbon domains. Both bands position and the bands intensity are highly susceptible for structural changes in the carbon
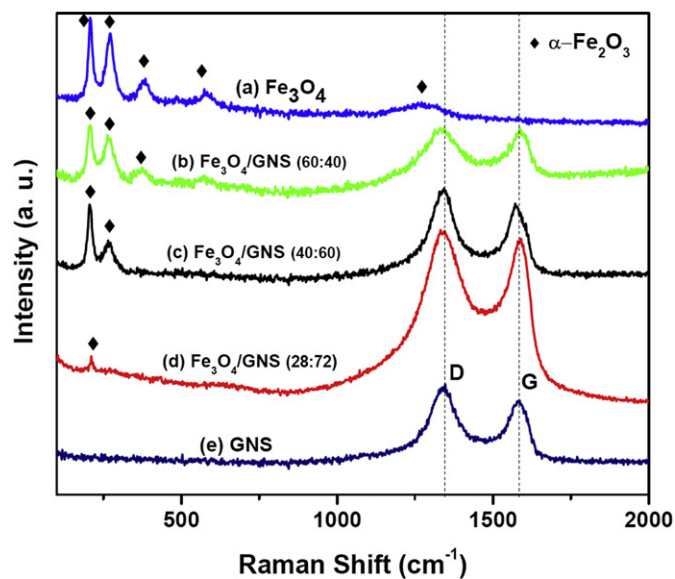
matrix. There are many factors, which can affect the position and intensity of the D and G bands, such as doping, layer numbers, defects, strains, substrate, etc [40−42]. Here, it could be clearly seen when increasing the Fe$_3$O$_4$ amount in the nanocomposite, the intensity of the lines corresponding to the Fe$_3$O$_4$ is increasing compared to D and G bands of graphene. The high intensity of D band than the G band for the nanocomposites and pure GNS indicates that more defect or highly disordered GNS and it is believed that highly disordered GNS would be a better support for anchoring Fe$_3$O$_4$ nanoparticles on the surface.

The amount of Fe$_3$O$_4$ anchored on the GNS in the nanocomposites was estimated using TG profile between 25 and 800 °C in air. In Fig. 3, the TG profiles of nanocomposites prepared at different Fe$_3$O$_4$/GNS ratio are shown. All the nanocomposites show a clear weight loss from 400 °C to 500 °C regions owing to the
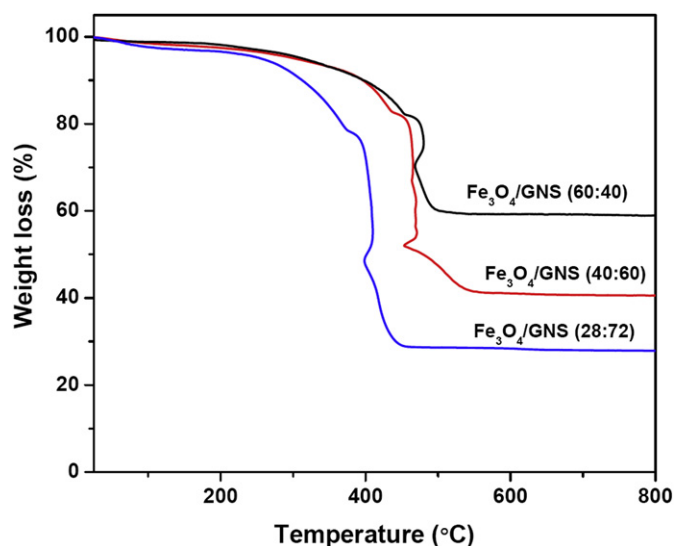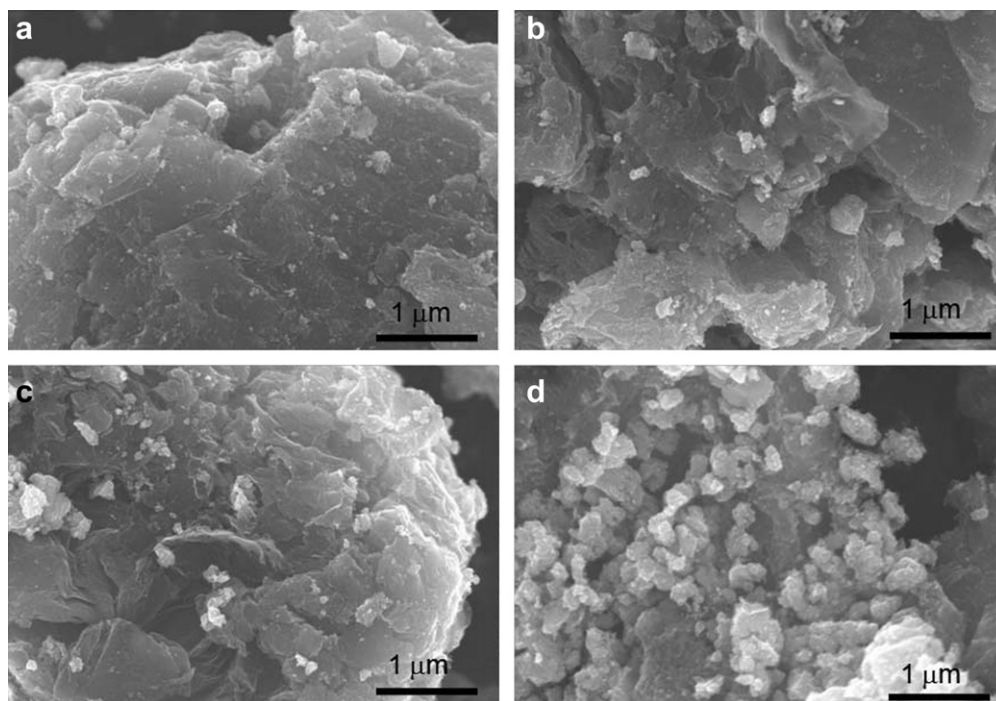

Fig. 3. TG profiles of Fe$_3$O$_4$/GNS nanocomposites with 60:40, 40:60 and 28:72 weigh ratios.

Fig. 4. FE-SEM images of Fe_3O_4/GNS nanocomposites with weight ratios of (a) 28:72, (b & c) 40:60 and (d) 60:40.

decomposition of GNS. Fe_3O_4/GNS ratio in the nanocomposites is estimated as 60:40, 40:60 and 28:72, the calculated ratios are in line with the amount of precursors used in the initial preparation. However, the decomposition profile corresponding to the lower amount of Fe_3O_4 (28:72) shows weight loss at lower temperature than the other two nanocomposites. It is well known that the GO will decompose at lower temperature than the GNS. The low temperature decomposition of GNS hints that the GNS has additional functional groups (unreduced or un-utilized by Fe_3O_4) due to the lower concentration of Fe_3O_4. The higher diffraction line intensity observed in the XRD for the Fe_3O_4/GNS (28:72) nanocomposite supports to our above speculation.

To investigate the morphology of the resulting Fe_3O_4/GNS nanocomposite, field emission scanning electron microscopy (FE-SEM) images were taken at different magnifications. Fig. 4 shows the representative FE-SEM images of Fe_3O_4/GNS nanocomposite with different weight ratios. Fig. 4b and c shows the FE-SEM images of Fe_3O_4/GNS (40:60) nanocomposite. The presence of Fe_3O_4 nanoparticles could be seen on the surface of the GNS. By comparing the images Fig. 4a and d corresponding to Fe_3O_4/GNS (28:72) and Fe_3O_4/GNS (60:40) nanocomposites respectively, it is clear that when the weight ratio changes the amount of Fe_3O_4 on GNS also changes drastically. This clearly indicates that Fe_3O_4 nanoparticles are well dispersed on the GNS irrespective to their concentration.

The morphology and particle size of the prepared nanocomposites have been further analyzed using TEM microscopy and shown in Fig. 5. The TEM images of nanocomposites observed for different Fe_3O_4 loading show a clear version of the nanoparticle distribution on GNS support. When the Fe_3O_4 weight increases in the nanocomposites the presence of agglomerated Fe_3O_4 nanoparticles on the GNS surface could be seen clearly by comparing images in Fig. 5a–d. At lower Fe_3O_4 loading (28:72, Fig. 5a), the GNS surface does not have much Fe_3O_4 nanoparticles. When the amount of Fe_3O_4 slightly increased (40:60, Fig. 5b and c), the Fe_3O_4 nanoparticles almost cover the entire surface and distributed uniformly

on the GNS. The particle size of Fe_3O_4 nanoparticles on the GNS was calculated from the TEM images and the calculated particles size are ∼10−20 nm, which is in good agreement with the crystallite size calculated from the XRD studies. However, formation of larger size Fe_3O_4 nanoparticles could be seen when, Fe_3O_4 loading increases to 60:40 (Fig. 5d), due to the agglomeration of nanoparticles and the GNS surface was completely covered.

The electrochemical properties of the Fe_3O_4/GNS nanocomposites have been investigated with galvanostatic charge/discharge measurements and cyclic voltammetry (CV) analysis. Fig. 6A shows the charge−discharge profiles of the nanocomposites with different Fe_3O_4/graphene ratio at the current density of 50 mA g^{-1}. It could be clearly seen that the capacity increases from 505 mAh g^{-1} to 930 mAh g^{-1}, when increasing Fe_3O_4/GNS weight ratio in the nanocomposite from 28:72 to 40:60. However, the amount of Fe_3O_4 in the Fe_3O_4/GNS nanocomposite increased further as 60:40 ratio, the capacity decreases drastically and 365 mAh g^{-1} was attained (Fig. 6A) similar to bulk Fe_3O_4 nanoparticles. Thus, it is believed that the amount of Fe_3O_4 nanoparticles on the GNS has significant influence on the capacity. Fe_3O_4/GNS nanocomposite with 40:60 weight ratio was selected and analyzed further. Fig. 6B shows the discharge capacity of Fe_3O_4/GNS, pure Fe_3O_4 nanoparticle (prepared via same experimental condition) and GNS without Fe_3O_4 nanoparticles. Though, the Fe_3O_4 nanoparticle (Fig. 6B) shows very high first irreversible discharge capacity of 1663 mAh g^{-1} than the Fe_3O_4/GNS (40:60) nanocomposite (1545 mAh g^{-1}), large capacity fading was observed in the subsequent cycles and, the capacity becomes ∼179 mAh g^{-1} and ∼51 mAh g^{-1} after 5 and 50 cycles, respectively. Whereas, the Fe_3O_4/GNS nanocomposites show stable reversible capacity ∼850−900 mAh g^{-1} and even after 50 cycles a reversible capacity of 675 mAh g^{-1} is retained (∼72% capacity retention compared to 2nd discharge). This clearly indicates that the addition of GNS in the Fe_3O_4 nanoparticles greatly enhances Li-ion storage. Further, the pure GNS shows a reversible capacity of ∼580 mAh g^{-1} in the initial cycles and gradually decrease to 323 mAh g^{-1} after 50 cycles
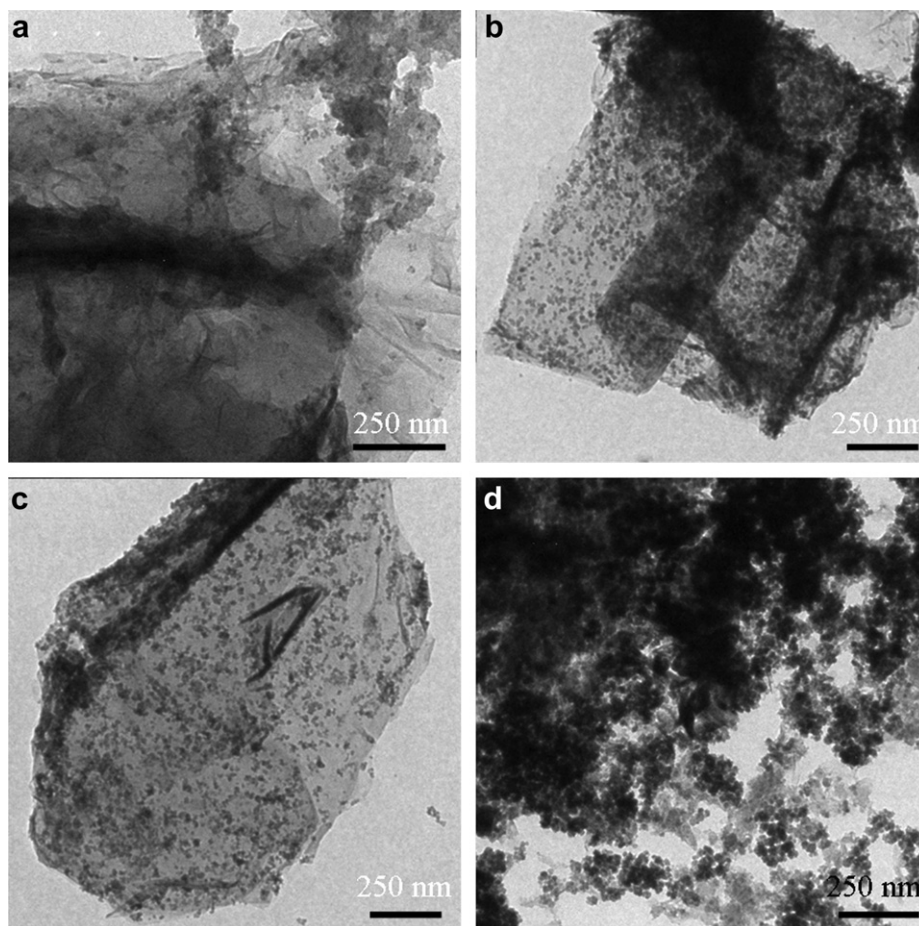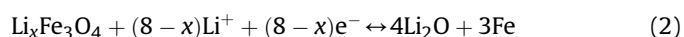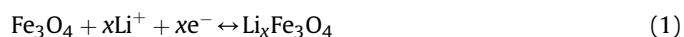
Fig. 5. Representative TEM images of Fe_3O_4/GNS nanocomposites with the weight ratios of (a) 28:72, (b & c) 40:60 and (d) 60:40.

(Fig. 6B). The reversible capacity of the Fe_3O_4/GNS nanocomposites is much higher than its individual counter parts at any point of time that indicates that the Fe_3O_4 anchoring on GNS enhances the Li-ion storage due to synergetic effect.

Fig. 6C shows the discharge–charge profiles of Fe_3O_4/GNS (40:60) nanocomposite at 1st, 2nd, 10th, 25th and 50th cycles. The first discharge voltage profile shows a steep voltage drop from about 2.0 to 0.85 V, which can be attributed to Li ion insertion in to the Fe_3O_4 nanoparticles as shown in Eqn (1) [43,44]. Then a long voltage plateau was observed at 0.85 V vs Li/Li$^+$ corresponding to the conversion reaction that results the formation of Li_2O and Fe as shown in Eqn (2) [43,44]. Later, a sloping curve from 0.85 V down to the cutoff voltage of 0.001 V, indicating typical characteristics of voltage trends for graphene composite electrodes attributed to the reversible reaction between lithium and graphene sheets (Eqn. (3)) and the formation of a solid electrolyte interphase (SEI) film. The voltage plateau observed for the nanocomposite electrodes is in good correspondence with the literature reported iron oxide/carbon nanocomposites [26–31]. The initial capacity loss for Fe_3O_4/GNS (40:60) might be due to the incomplete conversion reaction and irreversible lithium loss due to the formation of SEI layer [27,45,46]. Indeed, Fe_3O_4/GNS nanocomposite shows a high reversible charge–discharge capacity with a columbic efficiency of 98% for 50 cycles. (Fig. 6D). This could be explained based on the possible synergic effect that is (i) due to the Fe_3O_4 nanoparticles decoration on graphene surface durable the re-stacking of GNS greatly as a result more graphene surface will be available for Li-ion storage. Thus, the actual Li-ion storage in GNS will be higher
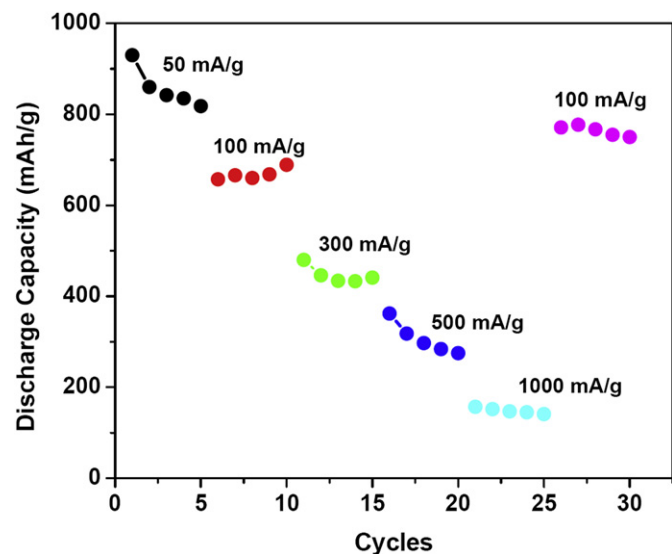
than the graphite (372 mAh g^{-1}), this argument was supported by earlier reported results [23]. (ii) The homogeneous dispersion of Fe_3O_4 nanoparticle on highly conducting graphene support offers enhanced cyclic performance due reduced Li-ion diffusion length and high conductivity of the graphene support.

$$Fe_3O_4 + xLi^+ + xe^- \leftrightarrow Li_xFe_3O_4 \quad (1)$$

$$Li_xFe_3O_4 + (8-x)Li^+ + (8-x)e^- \leftrightarrow 4Li_2O + 3Fe \quad (2)$$

$$C + xLi^+ + xe^- \leftrightarrow Li_xC \quad (3)$$

The rate dependent capacity performance of Fe_3O_4/GNS (40:60) electrodes was carried out at different current densities (50, 100, 300, 500 and 1000 mA g^{-1}) and shown in Fig. 7. It could be seen that at lower current densities 50 mA g^{-1} and 100 mA g^{-1}, the capacity is above 850 mA g^{-1} and 650 mA g^{-1}, respectively. Increasing current density 300, 500 and 1000 mA g^{-1} results significant decrease in the capacity. This could be attributed due to the poor electrical contact between the electrode materials and Ni mesh current collector and that would decrease the capacity due to high resistance at high current rates. Thus, the current density of the cell decreased again to 100 mA g^{-1} and the capacity values become similar to the original capacity observed at 100 mA g^{-1} during the initial cycles. This clearly indicates that the conductivity of the Fe_3O_4 nanoparticle decorated on the GNS does not effect and the resistance between the electrode materials and Ni mesh current collector is limiting the high capacity at high current densities.
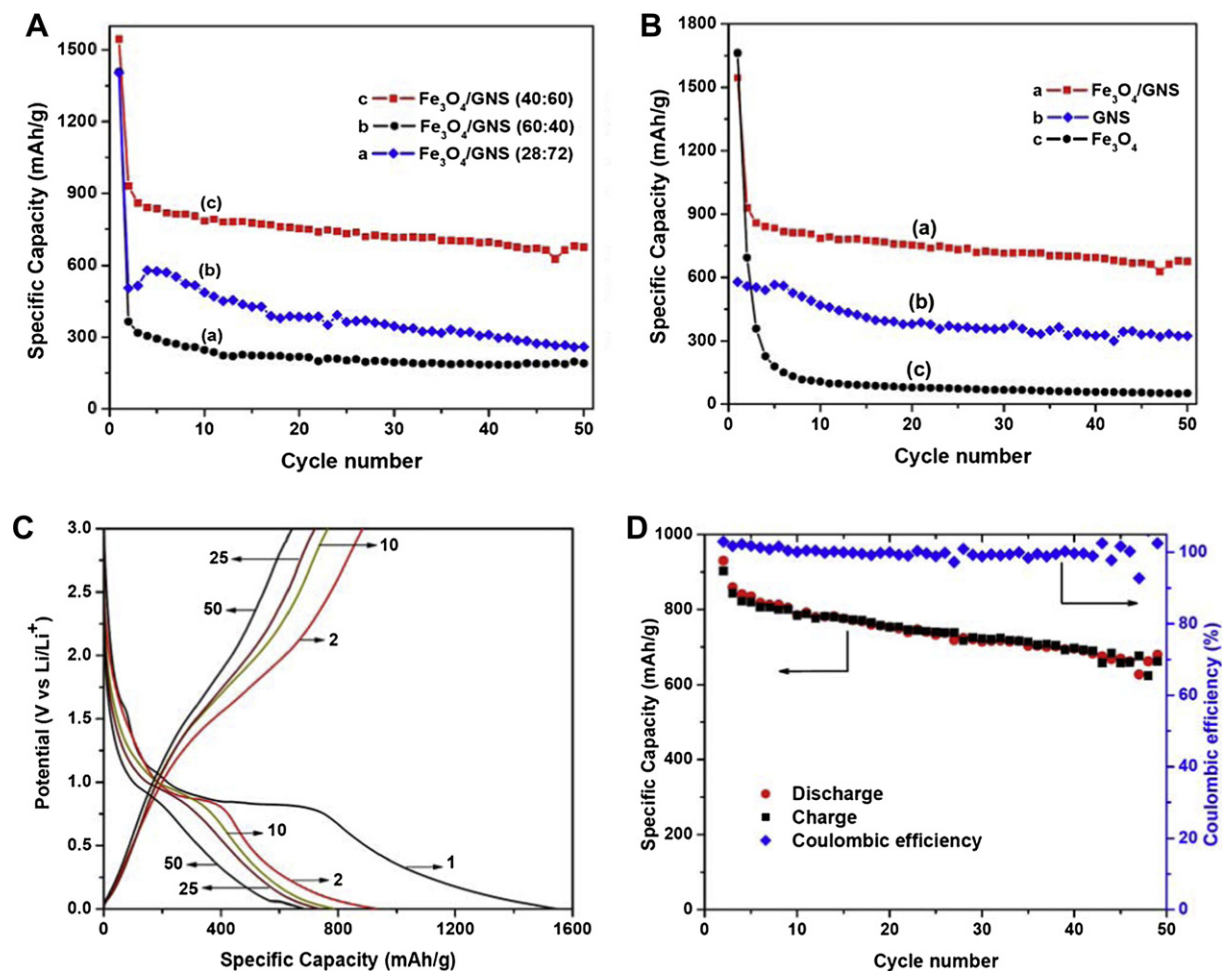
Fig. 6. Galvanostatic discharge capacity profiles of (A) Fe_3O_4/GNS nanocomposites with different weight ratios, (B) (a) Fe_3O_4/GNS nanocomposites, (b) pure GNS and (c) Fe_3O_4 nanoparticles at 50 mA g^{-1} current density. (C) Galvanostatic charge–discharge profile of Fe_3O_4/GNS (40:60) nanocomposite at different cycles. (D) Charge–discharge capacity and coulombic efficiency of Fe_3O_4/GNS (40:60) nanocomposites electrodes for 50 cycles.

To understand the Li-ion insertion and extraction process in the nanocomposites electrodes during discharge and charge process, cyclic voltammogram (CV) was measured between 0.001 V and 3 V vs Li/Li$^+$ at the scan rate of 0.1 mV s^{-1}. Fig. 8 shows the cyclic

Fig. 7. Cycling performance of Fe_3O_4/GNS (40:60) nanocomposite electrode at various current densities of 50 mA g^{-1}, 100 mA g^{-1}, 300 mA g^{-1}, 500 mA g^{-1} and 1000 mA g^{-1}.
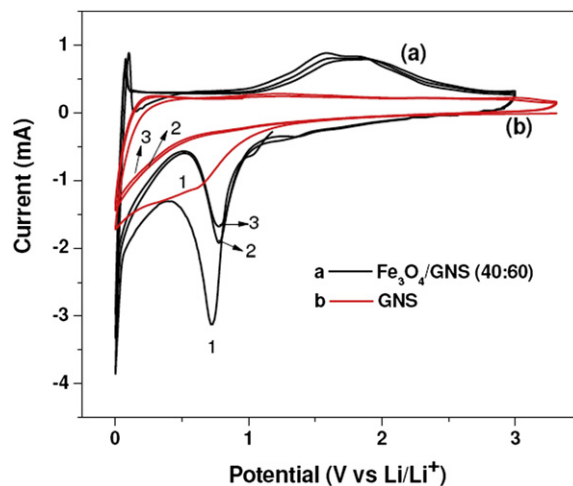
Fig. 8. Cyclic voltammetry profiles of (a) Fe_3O_4/GNS (40:60) nanocomposite, and (b) pure GNS electrodes at 0.1 mV s^{-1} scan rate.

voltammetery profile for first three cycles of nanocomposite electrodes and pure GNS (prepared using the same experimental condition). The peak observed below 0.2 V for the both electrodes indicates that reversible Li-ion intercalation in GNS (Equation (3)). The Fe_3O_4/GNS nanocomposite shows a characteristic peaks at 0.75 V, owing to the conversion reaction that results the formation of Li_2O and Fe as shown in Eqn (2). This peak is in good correspondence with the stable plateau observed at the same potential in the charge–discharge profile. However, this peak slightly shifts to higher voltage 0.80 V in the subsequent cycles, indicates that structural changes occur in the Fe_3O_4 nanoparticles after the Li-ion insertion in the first cycle and observed decreases in the peak intensity indicate the irreversible Li-ion loss due to SEI formation during the first cycle [4,28,44]. But, the peak intensity difference between the 2nd and 3rd cycle is very small, indicating the high capacity reversibility in the subsequent cycles.

4. Conclusions

Nanocrystalline Fe_3O_4/GNS nanocomposites were successfully prepared using hydrothermal method. The presence of face centered cubic Fe_3O_4 nanocrystalline particles in the Fe_3O_4/GNS, nanocomposite was revealed by XRD pattern. The weight ratio between the Fe_3O_4 and GNS in the prepared nanocomposites was estimated using TG profiles. SEM and TEM studies on the nanocomposites elucidate the homogeneous anchoring of Fe_3O_4 nanoparticles on the GNS surface when the weight ratio of the composites was 28:72 and 40:60. When the amount of Fe_3O_4 is high (60:40), homogeneous nature missing and presence of excess Fe_3O_4 nanoparticles were observed. The Raman spectroscopy confirms the co-existence of GNS and Fe_3O_4 nanoparticle in the nanocomposites, and the laser mediated decomposition or transformation of Fe_3O_4 to α-Fe_2O_3 was shown. The charge–discharge studies on the nanocomposite (40:60) indicate the high reversible Li-ion storage capacity with enhanced cycle life and high columbic efficiency. The fast capacity fading for the nanocomposites with 60:40 weight ratio of Fe_3O_4/GNS in the subsequent cycles reveals the bulk Fe_3O_4 nanoparticle like behavior owing to the high amount of Fe_3O_4 in the nanocomposites. Studies on the cyclic voltammetry confirm the reversible Li-ion storage in Fe_3O_4 nanoparticles anchored on GNS and GNS surface by conversion reaction mechanism and intercalation reaction, respectively.

Acknowledgment

References

[1] J.B. Goodenough, Y. Kim, Chem. Mater. 22 (2010) 587–603.
[2] P.G. Bruce, B. Scrosati, J.M. Tarascon, Angew. Chem. Int. Ed. 47 (2008) 2930–2946.
[3] N.S. Choi, Y. Yao, Y. Cui, J. Cho, J. Mater. Chem. 21 (2011) 9825–9840.
[4] P. Poizot, S. Laruelle, S. Grugeon, L. Dupont, J.M. Tarascon, Nature 407 (2000) 496–499.
[5] T.J. Kim, C. Kim, D. Son, M. Choi, B. Park, J. Power Sources 167 (2007) 529–535.
[6] T. Momma, N. Shiraishi, A. Yoshizawa, T. Osaka, A. Gedanken, J. Zhu, L. Sominski, J. Power Sources 97-98 (2001) 198–200.
[7] M. Muruganandham, R. Amutha, M. Sathish, T.S. Singh, R.P.S. Suri, M. Sillanpää, J. Phys. Chem. C 115 (2011) 18164–18173.
[8] R. Amutha, M. Muruganandham, M. Sathish, S. Akilandeswari, R.P.S. Suri, E. Repo, M. Sillanpää, J. Phys. Chem. C 115 (2011) 6367–6374.
[9] X. Zhu, Y. Zhu, S. Murali, M.D. Stoller, R.S. Ruoff, ACS Nano 5 (2011) 3333–3338.
[10] G. Derrien, J. Hassoun, S. Panero, B. Scrosati, Adv. Mater. 19 (2007) 2336–2340.
[11] J. Hassoun, G. Derrien, S. Panero, B. Scrosati, Adv. Mater. 20 (2008) 3169–3175.
[12] H.K. Liu, Z.P. Guo, J.Z. Wang, K. Konstantinov, J. Mater. Chem. 20 (2010) 10055–10057.
[13] M.S. Islam, C.R.A. Catlow, J. Solid State Chem. 77 (1988) 180–189.
[14] L. Taberna, S. Mitra, P. Poizot, P. Simon, J.M. Tarascon, Nat. Mater. 5 (2006) 567–573.
[15] H. Liu, G.X. Wang, J.Z. Wang, D. Wexler, Electrochem. Commun. 10 (2008) 1879–1882.
[16] W.M. Zhang, X.L. Wu, J.S. Hu, Y.G. Guo, L.J. Wan, Adv. Funct. Mater. 18 (2008) 3941–3946.
[17] A.K. Geim, Science 324 (2009) 1530–1534.
[18] A.K. Geim, K.S. Novoselov, Nat. Mater. 6 (2006) 183–191.
[19] G. Zhou, D.W. Wang, F. Li, L. Zhang, N. Li, Z.S. Wu, L. Wen, G.Q. Lu, H.M. Cheng, Chem. Mater. 22 (2010) 5306–5313.
[20] H. Kim, D.H. Seo, S.W. Kim, J. Kim, K. Kang, Carbon 49 (2011) 326–332.
[21] Z.S. Wu, W. Ren, L. Wen, L. Gao, J. Zhao, Z. Chen, G. Zhou, F. Li, H.M. Cheng, ACS Nano 4 (2010) 3187–3194.
[22] J. Su, M. Cao, L. Ren, C. Hu, J. Phys. Chem. C 115 (2011) 14469–14477.
[23] S.M. Paek, E.J. Yoo, I. Honma, Nano Lett. 9 (2009) 72–75.
[24] H. Kim, S.W. Kim, Y.U. Park, H. Gwon, D.H. Seo, Y. Kim, K. Kang, Nano Res. 3 (2010) 813–821.
[25] X. Huang, X. Zhou, L. Zhou, K. Qian, Y. Wang, Z. Liu, C. Yu, ChemPhysChem 12 (2011) 278–281.
[26] G. Zhou, D.W. Wang, F. Li, L. Zhang, N. Li, Z.S. Wu, L. Wen, G. Qing (Max) Lu, H.M. Cheng, Chem. Mater. 22 (2010) 5306–5313.
[27] X. Li, X. Huang, D. Liu, X. Wang, S. Song, L. Zhou, H. Zhang, J. Phys. Chem. C 115 (2011) 21567–21573.
[28] P. Lian, X. Zhu, H. Xiang, Z. Li, W. Yang, H. Wang, Electrochim. Acta 56 (2010) 834–840.
[29] M. Zhang, D. Lei, X. Yin, L. Chen, Q. Li, Y. Wang, T. Wang, J. Mater. Chem. 20 (2010) 5538–5543.
[30] L. Ji, Z. Tan, T.R. Kuykendall, S. Aloni, S. Xun, E. Lin, V. Battaglia, Y. Zhang, Phys. Chem. Chem. Phys. 13 (2011) 7170–7177.
[31] J.Z. Wang, C. Zhong, D. Wexler, N.H. Idris, Z.X. Wang, L.Q. Chen, H.K. Liu, Chem. Eur. J. 17 (2011) 661–667.
[32] W.S. Hummers, R.E. Offeman, J. Am. Chem. Soc. 80 (1958) 1339.
[33] L.J. Cote, F. Kim, J. Huang, J. Am. Chem. Soc. 131 (2009) 1043–1049.
[34] M. Sathish, S. Mitani, T. Tomai, A. Unemoto, I. Honma, J. Solid State Electrochem. 16 (2012) 1767–1774.
[35] B. Cullity, Elements of X-ray Diffraction, Addison-Wesley, Reading, MA, 1987, pp. 294.
[36] F.J. Owens, J. Orosz, Solid State Commun. 138 (2006) 95–98.
[37] R. Abu Mukh-Qasem, A. Gedanken, J. Colloid Interf. Sci. 284 (2005) 489–494.
[38] L.M. Malard, M.A. Pimenta, G. Dresselhaus, M.S. Dresselhaus, Phys. Rep. 473 (2009) 51–87.
[39] A.C. Ferrari, J.C. Meyer, V. Scardaci, C. Casiraghi, M. Lazzeri, F. Mauri, S. Piscanec, D. Jiang, K.S. Novoselov, S. Roth, A.K. Geim, Phys. Rev. Lett. 97 (2006) 187401.
[40] S. Pisana, M. Lazzeri, C. Casiraghi, K.S. Novoselov, A.K. Geim, A.C. Ferrari, F. Mauri, Nat. Mater. 6 (2007) 198–201.
[41] B. Das, R. Voggu, C.S. Rout, C.N.R. Rao, Chem. Commun. (2008) 5155–5157.
[42] A. Das, B. Chakraborty, A.K. Sood, Bull. Mater. Sci. 31 (2008) 579–584.
[43] L. Wang, Y. Yu, P.C. Chen, D.W. Zhang, C.H. Chen, J. Power Sources 183 (2008) 717–723.
[44] S. Wang, J. Zhang, C. Chen, J. Power Sources 195 (2010) 5379–5381.
[45] M.V. Reddy, T. Yu, C.H. Sow, X. Shen, C.T. Lim, G.V.S. Rao, Adv. Funct. Mater. 17 (2007) 2792–2799.
[46] Y. He, L. Huang, J.S. Cai, X.M. Zheng, S.G. Sun, Electrochim. Acta 55 (2010) 1140–1144.